COMMUNICATIONS PHYSICS

ARTICLE

https://doi.org/10.1038/s42005-019-0141-9 OPEN

Pressure-induced magnetovolume effect in CoCrFeAl high-entropy alloy

Lei Liu[1], Shuo Huang[2], Levente Vitos[2,3,4], Minjie Dong[5], Elena Bykova[6], Dongzhou Zhang[7], Bjarne S.G. Almqvist[1], Sergey Ivanov[8,9], Jan-Erik Rubensson[5], Bela Varga[10], Lajos K. Varga[11] & Peter Lazor[1]

High-entropy alloys (HEAs) composed of multiple-principal elements with (nearly) equimolar ratio establish a new conceptual framework for alloy design and hold a promise for extensive applications in industry, akin to the controlled expansion alloys (CEAs), such as Invar alloys. Spontaneously, one question emerges - would it be possible to synthesize a novel class of alloys combining the virtues of both CEAs and HEAs? Here, we report the pressure-induced magnetovolume effect in the body-centered-cubic CoCrFeAl HEA coupled with magnetic phase transitions from ferromagnetic to paramagnetic, and to non-magnetic states, originating from the successive collapses of local magnetic moments of Co and Fe. The observed magnetovolume anomalies, occurring in a progressive way, tailor appreciably the coefficient of thermal expansion of CoCrFeAl. These results further strengthen HEAs' anticipated potential for designing multifunctional materials in virtue of their multiple outstanding properties, and reveal possible routes for their future synthesis.

[1] Department of Earth Sciences, Uppsala University, 75236 Uppsala, Sweden. [2] Applied Materials Physics, Department of Materials Science and Engineering, Royal Institute of Technology, 10044 Stockholm, Sweden. [3] Department of Physics and Astronomy, Division of Materials Theory, Uppsala University, 75120 Uppsala, Sweden. [4] Institute for Solid State Physics and Optics, Wigner Research Centre for Physics, Budapest H-1525, Hungary. [5] Department of Physics and Astronomy, Division of Molecular and Condensed Matter Physics, Uppsala University, 75120 Uppsala, Sweden. [6] Photon Science, DESY, PETRA III, 22607 Hamburg, Germany. [7] Partnership for Extreme Crystallography, University of Hawaii at Manoa, Honolulu, HI 96822, USA. [8] Department of Engineering Sciences, Uppsala University, 75121 Uppsala, Sweden. [9] Department of Inorganic Materials, Karpov's Institute of Physical Chemistry, Vorontsovo pole, Moscow, Russia 105046. [10] Department of Materials Sciences, Transilvania University, 500036 Brasov, Romania. [11] Wigner Research Center for Physics of Hung. Acad. Sciences, PO Box 49Budapest 1525, Hungary. Correspondence and requests for materials should be addressed to L.L. (email: lei.liu@geo.uu.se) or to P.L. (email: peter.lazor@geo.uu.se)

Discoveries of new materials with excellent properties promoted the advancements of civilization. Metals and their alloys, in particular, have been the dominating enabling sources for thousands of years. However, in order to develop new alloys, an ever-repeating strategy—mixing one principal metallic element with the addition of minor property-tuning elements—has been applied since the Bronze Age. In the perspective of positioning in the compositional phase diagram, conventional alloys have been confined to the vicinities of their uni-elemental corners until 2004, when Yeh et al.[1] and Cantor et al.[2] proposed a novel approach to design alloys composed of multiple-principal elements in a (nearly) equimolar ratio. This novel class of alloys has been coined as high-entropy alloys (HEAs), stressing the high-configuration-entropy effect, originally believed to represent the reason why HEAs crystallize into a chemically disordered simple structure (bcc, fcc, and hcp) rather than forming intermetallic compounds[1]. This revolutionary concept advances material scientists to the center—hitherto a no man's land—of the compositional phase diagram. The newly developed HEAs display superior properties compared to the conventional alloys, including an exceptional mechanical performance at cryogenic[3] and high temperatures[4], excellent strength[5], and high resistance to corrosion[6]. Also reported are their intriguing electronic[7], magnetic[8], superconducting[9], and catalytic[10] properties. Consequently, HEAs attract intense and increasing attention because of immense potential applications[11–13]. Nonetheless, the immaturity in the synthesis process and a lack of fundamental understanding of properties hinders HEAs from finding their way from laboratory to market, calling for further investigations.

Controlled expansion alloys (CEAs) are widely used when the thermal expansion of designed engineered structures needs to be critically considered. Among the CEAs, Invar alloys represent the most common ones. Invar alloys were discovered by Guillaume in 1897[14], and were characterized by anomalously small thermal expansion in a certain temperature range, i.e., Invar effect, which has various industrial applications. However, the underlying mechanism of the Invar effect still represents a longstanding controversy[15–19]. In an attempt to explain the effect, Weiss proposed the 2γ model where the unusual thermal expansion originating from the anharmonicity of the lattice vibration was compensated by the volume collapse of Fe atoms during the high spin to low-spin transition[15]. Later, Van Schilfgaarde et al.[16] considered that the usual thermal expansion was counteracted by a gradual volume decrease during the continuous transformation of the direction of magnetic moment—from the parallel to the non-collinear configuration. Nevertheless, both the 2γ and the non-collinear models attribute the Invar effect to the mutual dependence on magnetism and volume, the so-called magneto-volume effect.

Bearing the prominent properties of Invar alloys and HEAs in mind, an interesting question arises—is it possible to synthesize materials, which possess combined merits of both classes of these extraordinary alloys? In the present study, by employing the techniques of in situ high-pressure X-ray diffraction (XRD) and ab initio calculation, we report the observation of the magneto-volume effect in CoCrFeAl HEA. Upon hydrostatic compression, CoCrFeAl undergoes a magnetic moment collapse—from ferromagnetic (FM), to paramagnetic (PM), and to non-magnetic (NM) state—while retaining the bcc crystal structure throughout the entire experimental pressure range up to 61 GPa. Decompressing the NM state results in a direct transformation into the FM state. The volume collapse during the PM to NM phase transition is large enough to counteract the effect of anharmonicity of lattice vibrations, thus leading to a very small coefficient of thermal expansion (CTE). The magnetovolume effect in CoCrFeAl HEA turns out to be sensitive to the degree of non-hydrostaticity, and the magnetic phase transition pathways differ during the compression and decompression cycles. The results of this study show that the newly-emerged HEAs exhibit intriguing and potentially useful properties worth to be investigated further. They also reveal the future possibility of designing promising Invar high-entropy alloys (IHEAs), which combine outstanding properties of Invar alloy and HEAs.

Results

Stability of the bcc structure. The composition of the synthesized sample was analyzed by energy-dispersive X-ray fluorescence spectroscopy (EDS) method, and the results indicated the average composition is $Co_{0.249}Cr_{0.228}Fe_{0.240}Al_{0.282}$ (Supplementary Fig. 1), close to the nominal composition. For simplicity, we use nominal composition CoCrFeAl in the following discussion. Combining the diamond anvil cell (DAC) and synchrotron-based XRD techniques, the crystal-structure evolution of the CoCrFeAl HEA at high pressures was investigated up to 61 GPa using different pressure transmitting media (PTM, Ne, and NaCl). More information is provided in the Methods section. At ambient pressure, the CoCrFeAl HEA crystallizes in the single bcc phase. This bcc CoCrFeAl HEA remains stable up to 61 GPa during the complete cycles of compression and decompression, regardless of the type of PTM used (Figs. 1 and 2 and Supplementary Fig. 2). The typical XRD patterns at selected pressures in the hydrostatic run are shown in Fig. 1. All the diffraction peaks from the bcc CoCrFeAl HEA shift towards higher 2θ angles with increasing pressure, as expected from the pressure-induced volume reduction. Neither peak disappearance nor new peak growths were observed, except for the reflections from the Re gasket and Ne PTM. The ab initio calculation (Supplementary Fig. 3) predicts that the bcc CoCrFeAl is thermodynamically stable over the fcc and hcp structures up to 60 GPa at 300 K, consistent with the present experimental results.

Anomalous compressive behavior. Although the bcc lattice of CoCrFeAl has been found stable in three independent runs up to 61 GPa, its pressure (P)–volume (V) data points show subtle kinks (Fig. 2), especially at 41–50 GPa during the hydrostatic decompression. The existence of these kinks makes it impossible to fit the P–V data using one single equation of state (EOS) and indicates potential magnetic or electronic phase transitions of bcc CoCrFeAl at high pressures. To illustrate these kinks, the local bulk modulus ($K=-V(\mathrm{d}P/\mathrm{d}V)$) is calculated using the following procedure[20]: Every five adjacent experimental P–V data points were fitted linearly to get the slope ($\mathrm{d}P/\mathrm{d}V$) of the central point, and consequently the local bulk modulus. The calculated local bulk modulus as a function of pressure is displayed in Fig. 3a. Pronounced kinks stand out at ~12, ~21, ~24, and ~32 GPa. In addition, the anomalous diffraction peak width (full-width at half-maximum, FWHM) of the strongest (110) peak as a function of pressure (Fig. 3b) supports the existence of phase transitions. In high-pressure XRD experiments, the FWHM variation is mainly contributed by the micro-strain of the sample[21], especially for the present disordered and distorted HEAs sample. The observed peak width anomaly reflects the micro-strain evolution of CoCrFeAl upon compression, originating from the competition between the pressure-induced volume reduction and the free volume release during the potential phase transitions.

Magnetic phase transition. Previous investigations on iron-based alloys (FeAl alloy) indicate that chemically disordered alloys that exhibit larger volumes favor the FM state[22]. For the bcc CoCrFeAl HEA with the largest chemical disorder, the addition of the

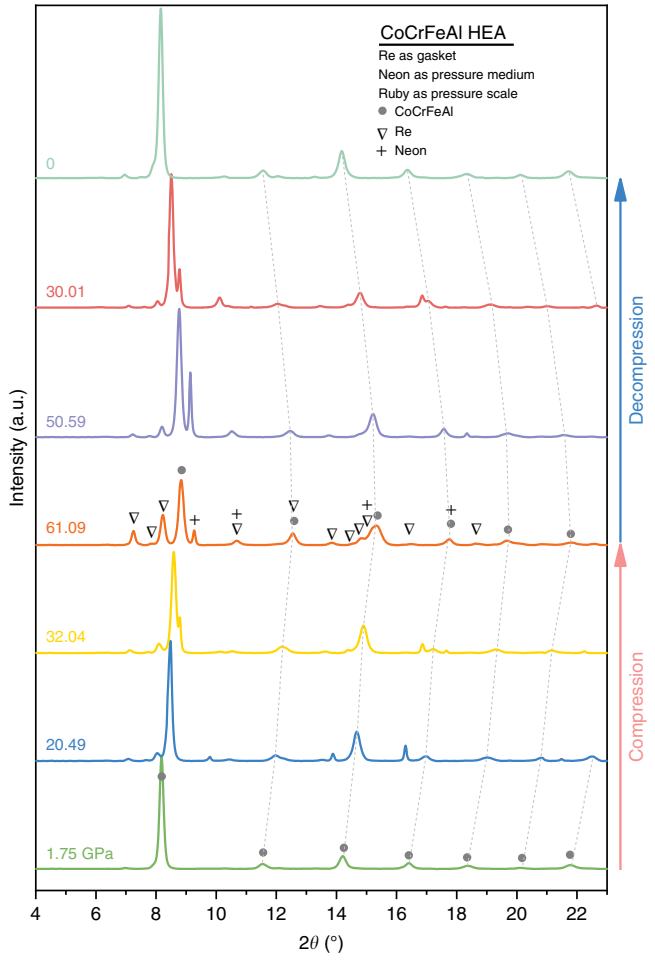

Fig. 1 X-ray diffraction (XRD) patterns of CoCrFeAl high-entropy alloy (HEA). In situ high-pressure XRD patterns collected during hydrostatic compression and decompression are presented. The labeled pressures are determined from the ruby fluorescence[36]. Solid dots, triangles, and pluses indicate the diffraction peaks from bcc CoCrFeAl HEA, Re gasket, and neon pressure medium, respectively. CoCrFeAl retains the bcc structure throughout the entire experimental runs.

large Al atom enlarges the free volume of Fe atoms. Moreover, a very recent theoretical calculation predicts that, upon the Al content increases, the CoCrFeNi-based HEA transforms from the PM state (fcc CoCrFeNi) to the FM state (bcc CoCrFeNiAl) at room temperature[23]. Consequently, for the bcc CoCrFeAl HEA that possesses both high Al content and large chemical disorder, the FM state at room temperature is expected.

Magnetic susceptibility measurements demonstrate that CoCrFeAl adopts a FM state at the ambient condition with the Curie temperature of ~470 K (Fig. 4). The performed theoretical calculations reveal a consistent result—the FM state represents the most stable state with the Curie temperature of ~500 K (Supplementary Figs. 3 and 4). For the sake of providing further insights into the FM properties of CoCrFeAl, the magnetic moment (Fig. 5a), electronic density of states (spin-polarized DOS, Fig. 6), and exchange interaction between alloy components (see Methods for detail, Supplementary Fig. 5) are also calculated. The ferromagnetism of CoCrFeAl mainly originates from the FM interactions of the nearest-neighbor Fe–Fe, Fe–Co, and Co–Co pairs (Supplementary Fig. 5). Al makes a negligible contribution to the magnetism of bcc CoCrFeAl, while the magnetic state of Cr is anti-FM and thus strongly destabilizes the FM order. Although the local magnetic moment of Cr is altered by the neighboring atoms[24], and the addition of Al may suppress the anti-FM order of Cr by altering its DOS near the Fermi level[25], the antiparallel Cr moments turn out to be primarily responsible for the small Curie temperature of the alloy compared to that of pure Fe and Co. The theoretical calculations are solely ab initio, without any experimental inputs.

To investigate the underlying mechanism of the compressive anomaly, the energy difference between the FM, PM, and NM states of bcc CoCrFeAl have been calculated. The results indicate that their energy differences decrease with increasing pressure (Supplementary Fig. 3a). Furthermore, the Curie temperature of the FM CoCrFeAl decreases with pressure and falls below room temperature at high pressure (~250 K at 60 GPa, Supplementary Fig. 4). Thus the FM to PM magnetic state phase transition is expected in CoCrFeAl at high pressure and room temperature according to the theoretical results. Upon further increase in pressure, the local magnetic moments of all the component atoms collapse to zero at ~60 GPa, i.e., the CoCrFeAl transforms to an NM state at higher pressures. This pressure-induced sequence of FM–PM–NM magnetic state transitions provides a viable explanation for the observed compressive anomaly in the present study. The isothermal EOS at 300 K of FM, PM, and NM phases of CoCrFeAl up to 60 GPa were calculated and are illustrated in Fig. 2. At corresponding pressures, the FM state occupies the largest average atomic volume while the NM state has the smallest one. Roughly, the experimental hydrostatic compression P–V data points agree with the calculated FM EOS at low pressure, the PM EOS at moderate pressure, and the NM EOS at high pressure (Fig. 2). In order to determine the equilibrium volume (V_0) and isothermal bulk modulus (K_0) at ambient pressure, experimental data points were fitted with the Vinet EOS[26]. In the pressure range of 0–10 GPa, the P–V data are well reproduced using $V_0 =$ 12.062 Å^3 per atom, $K_0 = 144.62$ GPa with its pressure derivative fixed at $K'_0 = 4$. Considering uncertainties, this experimental bulk modulus agrees reasonably well with the estimated values of 153.75 GPa using the additivity law[27]. In the pressure range of 50–61 GPa (the pure NM state), we obtain $V_0 = 11.727$ Å^3 per atom, $K_0 = 190.09$ GPa with K'_0 fixed at 4. These results demonstrate that the NM state has a smaller equilibrium volume. In the pressure range 0–43 GPa during decompression, the CoCrFeAl HEA adopts a pure FM state (as discussed below). The fitted EOS parameters are $V_0 = 12.019$ Å^3 per atom, $K_0 = 179.12$ GPa, and $K'_0 = 4.26$, consistent with the calculated EOS of the FM phase at 300 K ($V_0 = 12.047$ Å^3 per atom, $K_0 = 167.10$ GPa, and $K'_0 = 4.52$). These EOS parameters are listed in Table 1.

According to the above discussions, we suggest that CoCrFeAl undergoes a sequence of magnetic state phase transitions from FM state, to PM state, and to NM state under hydrostatic compression. However, upon the hydrostatic decompression, CoCrFeAl transfers from the NM state to FM state directly, omitting the PM state according to the isothermal EOS data (Fig. 2). Under non-hydrostatic compression, CoCrFeAl transforms from FM to PM state, without entering the NM state up to 55 GPa. During the following decompression, CoCrFeAl transforms back to the FM state below 42 GPa, signifying that the degree of non-hydrostaticity has a significant effect on the magnetic state transition of CoCrFeAl. The magnetic state transformation sequence under the non-hydrostatic condition is also confirmed by the experiment using NaCl as the PTM (Supplementary Fig. 2). The transition sequence of CoCrFeAl, along with magnetic moments calculated for the case of hydrostatic compression, is summarized in Fig. 5.

The pressure dependence of the local bulk modulus (Fig. 3a) and the diffraction peak width (Fig. 3b), both show that the magnetic state transition of CoCrFeAl HEA during the hydrostatic compression includes several steps. The onset pressures of

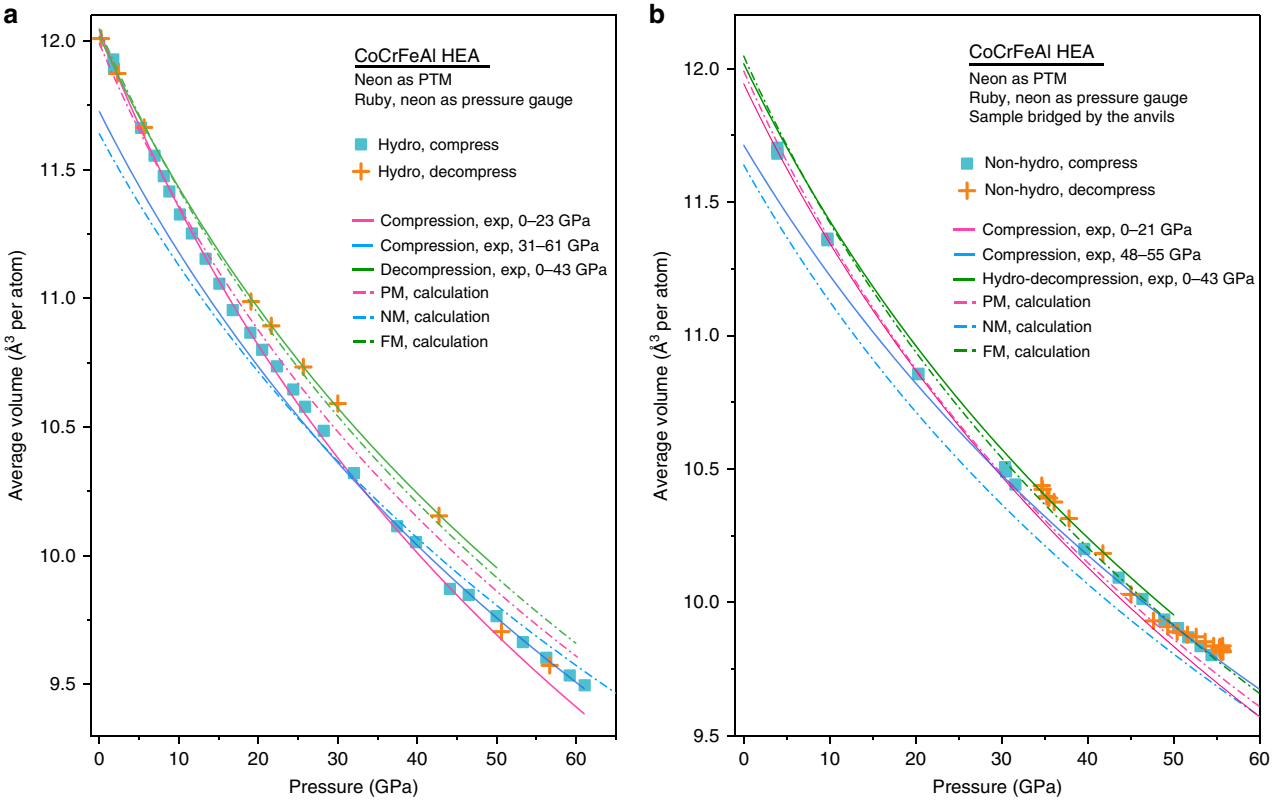

Fig. 2 Pressure dependence of the average atomic volume. The ruby fluorescence[36] and neon equation of state (EOS)[39] are used as a pressure gauge in the hydrostatic (**a**) and non-hydrostatic runs (**b**), respectively. The error bar of the measured average atomic volume is smaller than its symbol size. The hydrostatic volume data are fitted using the Vinet EOS in three different pressure ranges (solid lines). For comparison, the calculated EOSs of CoCrFeAl in ferromagnetic, paramagnetic, and non-magnetic states at 300 K are also presented (dash-dotted lines). The parameters of the EOS are listed in Table 1

the transition, visually read from Fig. 3a, b, are roughly consistent with each other. However, according to the procedure used to calculate the local bulk modus, four other adjacent data points affect the local bulk modulus at specific pressure, thus the phase transition pressure read from Fig. 3a lags behind the real transition pressure. Consequently, in the ensuing discussion, we use the onset pressures of the phase transition from Fig. 3b, which may reflect the phase transition instantly.

Interpreting the experimental observations with the help of ab initio calculations, we suggest that, under hydrostatic compression up to 61 GPa (Fig. 3a, b), the bcc CoCrFeAl HEA undergoes the following magnetic transitions in three stages:

In the pressure range 0–16 GPa, CoCrFeAl gradually transforms from the initial FM to PM state. From 0 to ~10 GPa, the alloy remains in the FM state. Both the local bulk modulus and FWHM of the (110) diffraction peak increase monotonically with increasing pressure. The pressure-induced micro-strain accounts for the diffraction peak width increase. From ~10 to ~16 GPa, the local bulk modulus decreases slightly to begin with, then increases again with increasing pressure, while the FWHM of the (110) diffraction peak remains constant. Such a pressure-induced lattice softening has also been reported in Fe–Ni[17] and $Cd_{1-x}Mn_xGeAs_2$[28] Invar alloys, originating from their magnetic structure relaxation[16]. Furthermore, the previous study[29] indicates that the Fe–Fe interatomic distance d_i controls the magnetic coupling between Fe atoms with the critical value of 2.45 Å: for d_i < 2.45 Å, the magnetic moments favor antiparallel coupling, whereas for d_i > 2.45 Å the preferred coupling is parallel. According to the present P–V data, the nearest-neighbor distance in bcc CoCrFeAl reaches 2.45 Å at around 10 GPa, from where the material gradually transforms from the FM to the PM state. At this stage, the population of the PM state increases at the expense of the FM state. Because the PM state has a smaller volume (Fig. 2), both the pressure effect and magnetic transition account for the volume decrease. The free volume release from the FM to PM state transition compensates the pressure-induced micro-strain in the sample, thus the diffraction peak width of the sample remains almost constant in this range. According to the DOS calculation, the most pronounced change across this FM to PM phase transition is that the partial density of states of Co becomes highly symmetric (Fig. 6). The high-spin (HS) to the low-spin (LS) transition causes a major magnetic moment decrease by 70% at 10 GPa, from $1.22\mu_B$ for HS to $0.37\mu_B$ for LS at 10 GPa (Fig. 5a). With further increases in pressure, the magnetic moment of Co vanishes at around 18 GPa. By comparison, the magnetic moment of Fe decreases by only 12% (from $2.00\mu_B$ to $1.76\mu_B$ at 10 GPa). Accordingly, the magnetovolume effect of CoCrFeAl in this range accompanies the HS to LS transition of Co, not Fe as proposed by the 2γ model[15].

In the second stage, spanning pressure range 16–31 GPa, a gradual transformation from the PM to the NM state takes place. From ~16 to ~23 GPa, the local bulk modulus decreases slowly with increasing pressure. However, the FWHM of the (110) diffraction peak increases steeply as a function of pressure. At this stage, the sample remains in the PM state. The pressure effect solely accounts for the volume decrease of the sample, and as the micro-strain in the sample increase quickly, so does the diffraction peak width. From ~23 to ~31 GPa, the local bulk modulus increases slowly with increasing pressure. In this pressure range, the FWHM of the (110) diffraction peak decreases drastically. Both the pressure effect and magnetic transition account for the volume decrease during this range. However, the

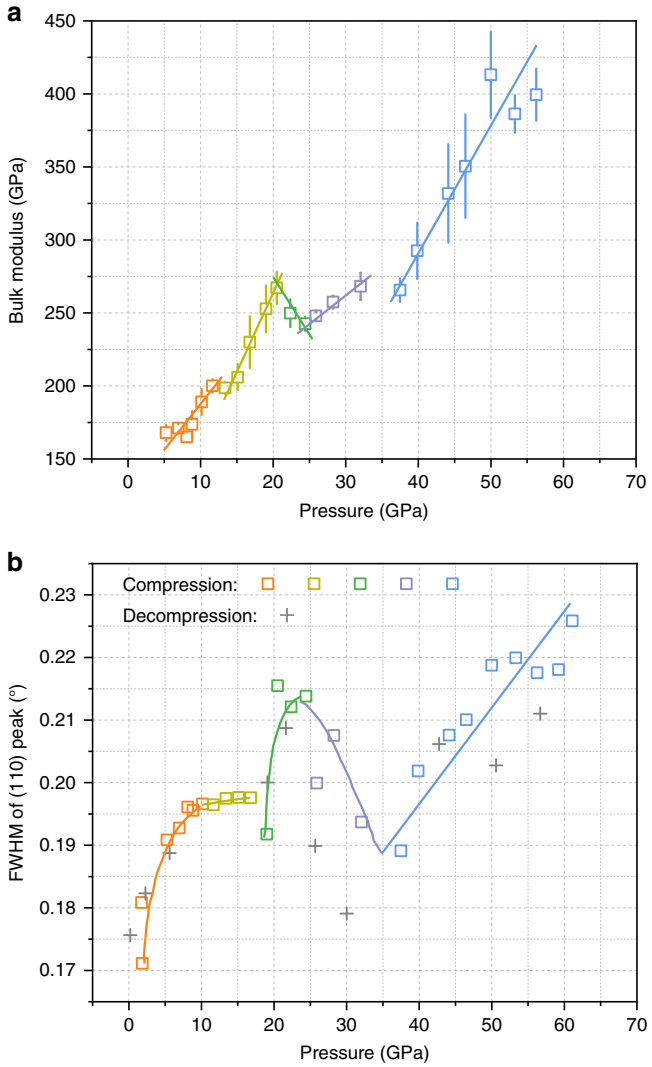

Fig. 3 Pressure dependencies of the bulk modulus and peak width. **a** Local bulk modulus. Colors of different symbols represent different magnetic states or phase transitions. The indicated uncertainties arises from the fitting error of dP/dV. The lines are guides for the eyes. **b** Full-width at half-maximum (FWHM) of the (110) diffraction peak of bcc CoCrFeAl high-entropy alloy (HEA). The error of the measured FWHM is comparable to the symbol size

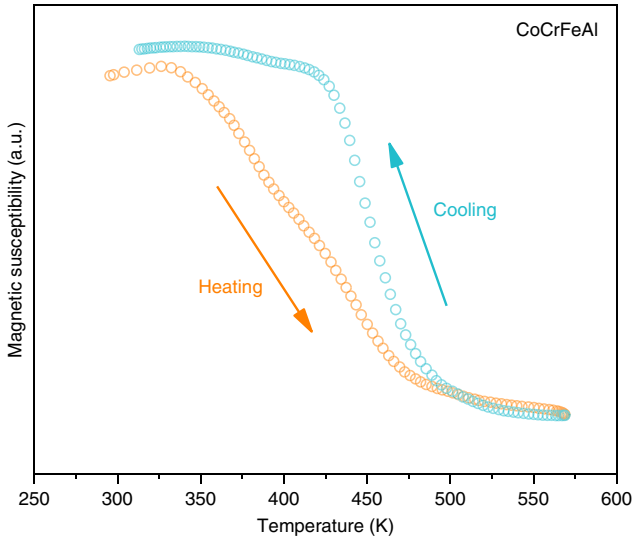

Fig. 4 Temperature dependence of the magnetic susceptibility of CoCrFeAl at ambient pressure. The orange and cyan symbols represent the data collecting during heating and cooling runs, respectively. Measurement error is smaller than the symbol size

micro-strain released by the magnetic transition is larger than that induced by the compression effect, which is why the peak width decreases overall. At this stage, the sample transforms from the PM to NM state. This transition is accompanied with a magnetic moment collapse of Fe (Fig. 5a) and contributes to the magnetovolume anomaly of CoCrFeAl in this pressure range.

Finally, in the pressure range 31–61 GPa, the alloy remains in the NM state. Both the local bulk modulus and FWHM of the (110) diffraction peak increase monotonically with increasing pressure. The material is in the pure NM state. Only the pressure effect accounts for the volume decrease of the sample, and as the micro-strain in the sample increases again, so does the diffraction peak width.

The observed FM–PM and PM–NM transitions are of the first order because of the associated volume reduction (Fig. 2). However, as it takes 6 and 8 GPa, respectively, to be completed, both transitions are sluggish. A similar sluggishness has been reported in the fcc to hcp transitions of CoCrFeMnNi HEA[30,31] and CoCrFeNi[32]. Tracy et al.[31] considered that the sluggish nature of transition in CoCrFeMnNi HEA originated from the rising energy barrier associated with stacking fault formation upon pressure increase, akin to the fcc to hcp phase transition of Ar. On the other hand, Zhang et al.[32] argued that a pressure-induced kinetic inhibition of the atomic motion caused the sluggish phase transition of CoCrFeAl at high pressure. However, in the present case of CoCrFeAl, no crystal lattice reconstruction is involved in the course of transition. We speculate that the sluggish nature of phase transition, not only structural phase transition, but also magnetic and/or electronic phase transitions, is a general phenomenon in HEAs and may arise from inherent properties of HEAs, for example, the local energy fluctuations originating from the intrinsic chemical disorder in HEAs[33].

Anomalous CTE at high temperatures. The ensuing question is how the volume collapse during the magnetic phase transition influences the CTE of CoCrFeAl HEA. To address this point, we measured the temperature dependence of the linear CTE up to 820 K (Fig. 7). The CTE of CoCrFeAl exhibits two deviations from a regular behavior: (1) from 430 to 720 K, the CTE remains almost a constant. We consider this anomaly arises from the FM–PM phase transition—the anharmonic lattice expansion is offset partly by the volume collapse during the FM–PM phase transition (Fig. 7). The upper temperature agrees reasonably well with the measured Curie temperature of CoCrFeAl (Fig. 4). (2) From 720 to 770 K, the CTE decreases with increasing temperature, reaching almost zero at around 770 K. Meanwhile, the sample length stays practically constant in the range 760–775 K (Fig. 7). This is reminiscent of an Invar effect. We interpret the second anomaly to originate from the PM–NM phase transition, in which the lattice expansion is counterbalanced entirely by the volume collapse during the magnetic transition. These results agree with the calculated equilibrium volume collapses during magnetic phase transitions at ambient pressure (Table 1). The FM–PM volume collapse is $\Delta V_1 = V_{FM} - V_{PM} = 0.056$ Å^3, while the PM–NM volume collapse is $\Delta V_2 = V_{PM} - V_{NM} = 0.352$ Å^3 which is about 6.3 times higher than ΔV_1.

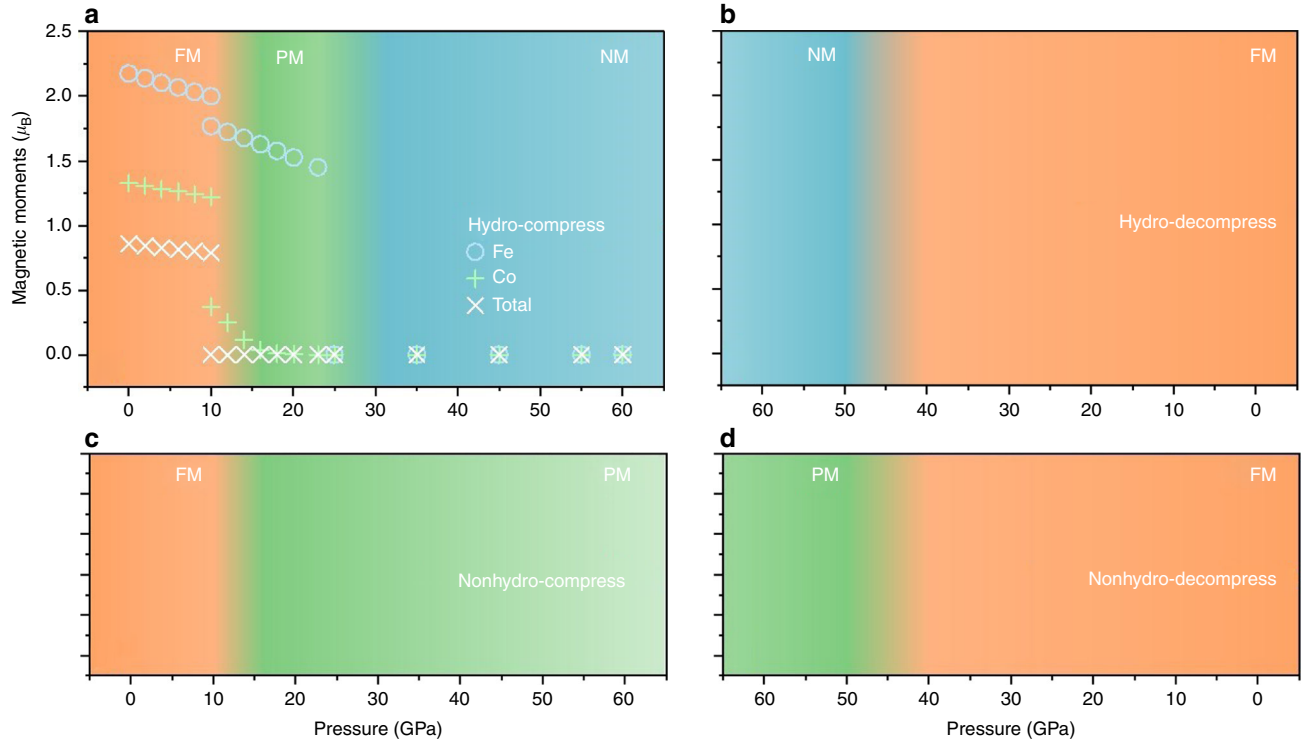

Fig. 5 Phase diagram of CoCrFeAl high-entropy alloy. **a** Phase transition under hydrostatic compression, from ferromagnetic (FM, orange) to paramagnetic (PM, green) to non-magnetic (NM, cyan). The calculated magnetic moments of Fe and Co, and the total magnetic moment are also shown. **b** Phase diagram under hydrostatic decompression. **c** Phase diagram under non-hydrostatic compression. **d** Phase diagram under non-hydrostatic decompression. All diagrams are at room temperature

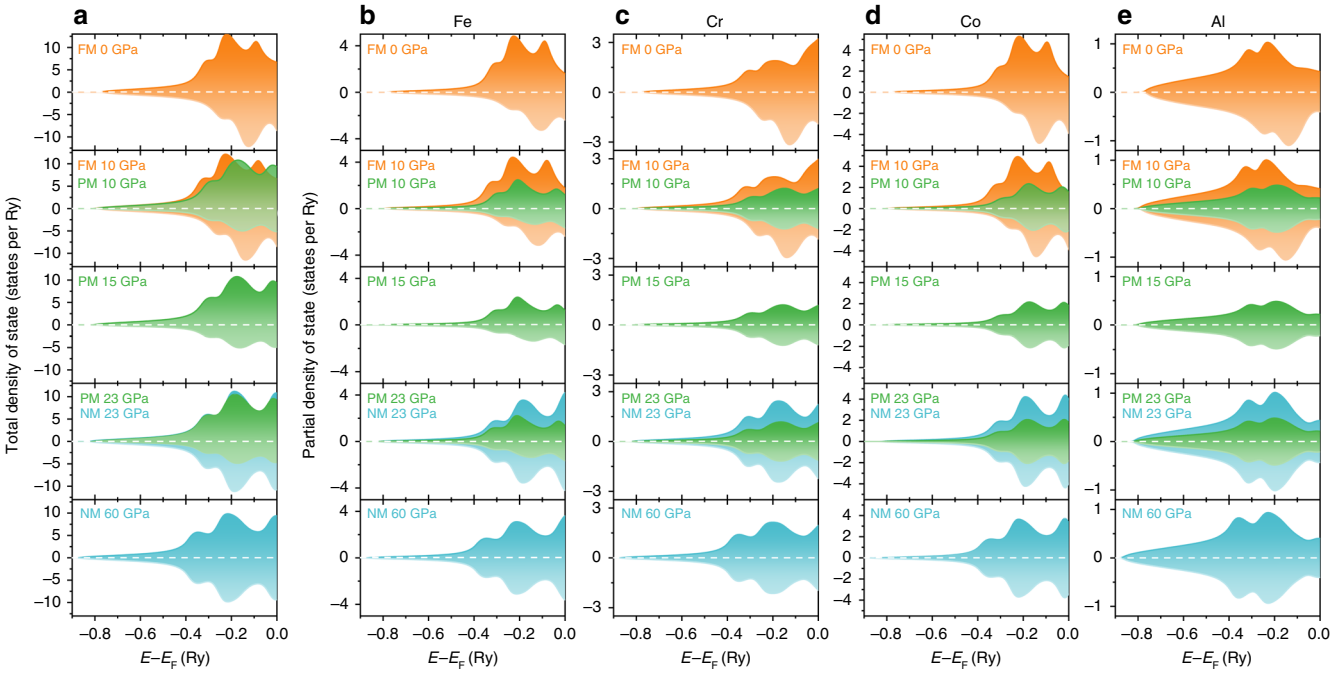

Fig. 6 The density of states. **a** Spin-polarized total density of states of CoCrFeAl high-entropy alloy in the bcc structure below the Fermi level (E_F). **b** Partial density of states (PDOS) of Fe. **c** PDOS of Cr. **d** PDOS of Co. **e** PDOS of Al. For PM state, partial densities of state for $Co^{\downarrow}$, $Cr^{\downarrow}$, $Fe^{\downarrow}$, and $Al^{\downarrow}$ are identical to those for $Co^{\uparrow}$, $Cr^{\uparrow}$, $Fe^{\uparrow}$, and $Al^{\uparrow}$ apart from the sign (spin up and spin down) difference

Hysteresis during the decompression and non-hydrostatic effect. The decompression behavior of CoCrFeAl is reversible in the high-pressure range (42–61 GPa), while it does not follow the same behavior as during compression in the lower pressure range (Fig. 2). In the low-pressure range of 0–42 GPa, the average atomic volume of the sample is larger during decompression than that during compression. The reason is that during compression and decompression, the sample possesses a different FM/PM ratio

Table 1 EOS parameters of CoCrFeAl

Run	V_0 (Å^3)	K_0 (GPa)	K_0'	Pressure range (GPa)
Calculation				
FM	12.047	167.1	4.52	
PM	11.991	163.6	4.69	
NM	11.639	201.7	4.41	
Experiment: Hydrostatic				
Compress	12.062	144.62	4 (fixed)	0–10
Compress	12.042	150.93	4 (fixed)	0–23
Compress	11.784	199.12	4 (fixed)	16–23
Compress	11.726	190.08	4 (fixed)	31–61
Decompress	12.019	179.12	4.26	0–43
Experiment: Non-hydrostatic				
Compress	11.944	176.13	4 (fixed)	0–21
Compress	11.713	215.90	4 (fixed)	48–60
Decompress	12.206	161.57	4 (fixed)	30–41

The experimental values are yielded by fitting the data points with Vinet EOS[26]:$P = 3K_0(V/V_0)^{-2/3}\left[1-(V/V_0)^{1/3}\right]exp\{1.5(K'_0-1)[1-(V/V_0)^{1/3}]\}$, where the V_0, K_0, and K_0' are the equilibrium volume, bulk modulus, and its pressure derivative at ambient pressure

at the same pressures—where a higher FM/PM ratio results in a larger volume. However, the volume difference decreases with decreasing pressure and almost vanishes at ambient pressure, indicating the sample returns fully to the FM state at ambient pressure. In the pressure range of 0–42 GPa, the P–V data during decompression can be well fitted by the Vinet EOS[26], with $V_0 =$ 12.019 Å^3 per atom, $K_0 = 179.12$ GPa, and its pressure derivative $K'_0 = 4.26$. The compression/decompression equilibrium volumes V_0 are mutually consistent. However, the isothermal bulk modulus K_0 and its pressure derivative are larger during decompression than their corresponding values obtained during compression.

As shown in Fig. 2, the average atomic volume of CoCrFeAl under non-hydrostatic compression is larger than that under hydrostatic compression. However, when decompressed to pressures below 42 GPa, the average atomic volumes determined from both hydrostatic and non-hydrostatic runs are mutually consistent. The pressure dependencies of the FWHM of the (110) diffraction peak under hydrostatic and non-hydrostatic compressions differ (Fig. 3b and Supplementary Fig. 6). These results can be understood by considering that different pathways are followed in the phase transitions, as shown in Fig. 5. In the hydrostatic run, the followed phase transition sequence reads FM–PM–NM, while upon decompression the NM state transforms directly into the FM state. On the other hand, in the non-hydrostatic run, the NM state is absent up to 55 GPa. These results indicate that not only the degree of hydrostaticity but also the compression/decompression history affects the pathways of the magnetic state transitions in CoCrFeAl HEA. The pressure hysteresis during compression and decompression implies that the PM and/or NM phases are metastable[34]. The phase transition pathways which involve metastable phases are substantially affected by the degree of hydrostaticity, the compression and decompression history, as well as rate, and sample condition (single crystal/powder, impurities) (see ref. [35] and references therein).

Discussion

The magnetovolume effect is discovered in CoCrFeAl HEA by in situ high-pressure XRD techniques with the assistance of ab initio calculations. The calculations reveal that the experimentally observed phase transitions are of magnetic origin and result from the collapse of local magnetic moments of Co and Fe. The large volume decrease during the PM to NM transition results in a dramatically reduced CTE at high temperature, evoking an Invar-like behavior, though only in a very narrow temperature range. Moreover, the FM to PM and the PM to NM phase transition temperatures can be pressure-tuned to the ambient temperature, suggesting a potential way of tuning the temperature range of the magnetovolume anomaly, and conceivably of the Invar effect. This work also reveals the possibility of designing and synthesizing extraordinary IHEAs in the future.

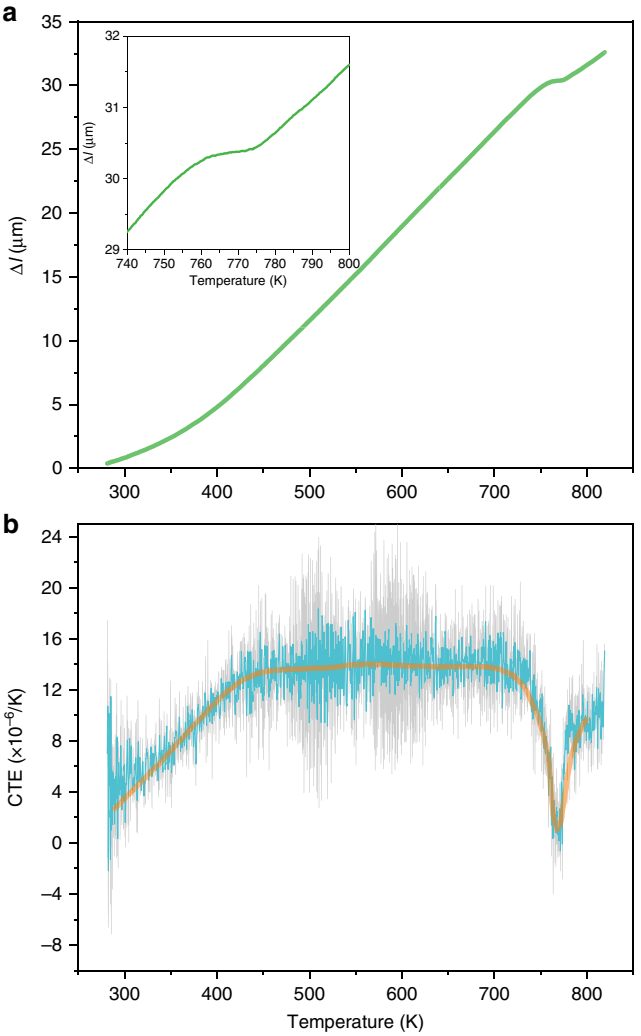

Fig. 7 Linear thermal expansion of CoCrFeAl. **a** Sample length change $\Delta l = l_t - l_0$ as a function of temperature. **b** Linear physical coefficient of thermal expansion (CTE) ($\alpha = (1/l_t)(d(l_t - l_0)/dt)$) as a function of temperature. The gray signal is the raw data and the cyan signal is the smoothed data. The orange line is a guide for the eyes

Methods

Synchrotron XRD. The CoCrFeAl HEAs with a nominal molar ratio were prepared by the arc melting method in a high purity argon atmosphere. The chemical composition and the homogeneity of the synthesized sample were examined by the EDS analysis (see Supplementary Fig. 1). Small fragments of CoCrFeAl were produced by scraping the synthesized bulk materials with a fine rasp, then a tiny piece of appropriate size (~30 μm) was selected, and loaded into the sample chamber of DAC. Three runs of in situ high-pressure XRD experiments were carried out under hydrostatic and non-hydrostatic conditions, respectively.

In the hydrostatic run, diamond anvils with 200 μm culet size were mounted on the symmetric cells to generate high pressure. The Re gasket with an initial thickness of 250 μm was indented to 30 μm, and a sample chamber with a diameter of 80 μm was drilled in the center of the pre-indented hole. The sample with a typical size of ~30 μm was loaded into the sample chamber, along with tiny ruby balls serving as pressure gauge[36] and neon as a PTM. The in situ high-pressure angle-dispersive XRD experiments were carried out at the Extreme Conditions Beamline (ECB) P02.2 (ref. [37]), PETRA III, Hamburg, Germany. The pressure in the sample chamber was varied using the membrane control system, and monitored by the online ruby system. The incident X-rays were monochromatized to 42.68 keV corresponding to a wavelength of 0.2905 Å. The beam was focused to a size of 1.25 μm (vertical) × 2.44 μm (horizontal) (FWHM) by Kirkpatrick–Baez mirrors. Two-dimensional diffraction images were collected using the fast area XRD 1621 (Perkin Elmer) 2D detector (2048 × 2048 pixels, 200 μm × 200 μm pixel size) with a typical exposure time of 30 s. The distance from the sample to the detector and the detector's geometric parameters were calibrated by the CeO_2 standard (674b from the National Institute of Standards).

Two independent non-hydrostatic runs were also performed in order to evaluate the effect of non-hydrostaticity. The DACs and the sample assemblies were similar to the hydrostatic run, although T301 stainless steel gaskets and different PTMs (neon and NaCl) were used. In the neon run, the sample chamber collapsed after the gas loading, causing the sample to bridge the anvils. The sample was thus compressed non-hydrostatically despite the presence of a soft PTM neon. These two runs of experiments were performed at the Advanced Photon Source of Argonne National Laboratory, beamline 13BM-C, GSECARS[38]. The incident X-ray beam was monochromatized to 28.57 keV (wavelength of 0.4340 Å) and focused to a spot size of 18 μm (vertical) × 12 μm (horizontal) (FWHM). The diffraction patterns were collected by the MAR165 CCD detector (2048 × 2048 pixels, 79 μm × 79 μm pixel size). The distance from the sample to the detector and the detector's geometric parameters were calibrated by the NIST 660a LaB_6 standard. The EOS of neon and NaCl[39] were used as pressure scales respectively in these two runs.

All the measurements were conducted at room temperature. The two-dimensional diffraction patterns were integrated by Dioptas[40] in order to obtain the 2θ–intensity curves for a further analysis. The software Fityk[41] was used to fit and resolve the overlapped diffraction peaks by applying the Voigt-profile peak function. The parameters of the EOS of CoCrFeAl in different states were determined by the EosFit7-GUI software[42].

Calculation. The present ab initio calculations were based on density functional theory[43] implemented in the framework of the exact muffin-tin orbitals formalism[44,45]. The single-electron equations were solved within the scalar-relativistic approximation and soft-core scheme. The exchange-correlation effects were treated within the generalized gradient approximation[46]. The chemical and magnetic disorders were taken into account using the coherent potential approximation[47–49]. The PM state was simulated by the disordered local moment model[50]. The Monte-Carlo simulations were based on the effective Heisenberg-like Hamiltonian, $H = -\sum_{i,j} J_{ij}\mathbf{m}_i \cdot \mathbf{m}_j$, where J_{ij} represents the strength of the magnetic exchange interaction between atomic sites i and j with magnetic moments $\mathbf{m}_i$ and $\mathbf{m}_j$. Further technical details can be found in the previous work[23,51].

Magnetic susceptibility measurements. The magnetic susceptibility of the sample was measured as a function of temperature, with an AGICO MFK1-FA Kappabridge equipped with a CS4 furnace. Temperature-dependent susceptibility measurements were made at room temperature up to 296 °C with average heating and cooling rates of 8.6 °C/min. The sample was exposed to an argon gas flow, providing an inert sample environment. An AC field with 200 A/m field strength and 976 Hz frequency was used for the measurements.

EDS analysis. EDS analyses were performed using a PANalytical Epsilon 3 XL ED-XRF spectrometer, equipped with a 50 kV Ag-anode X-ray tube, six filters, a helium purge facility, and a high-resolution silicon drift detector. The system was calibrated using a number of international and national certified reference materials. The analysis was done in an air atmosphere and the sample was exposed to X-ray for 600 s. The sample was transferred into a P1 cup assembled with a high transmission Prolene supporting foil. The sample was measured 10 times at 10 different spots on the sample consecutively.

Coefficient of thermal expansion measurement. A Linseis-L 75/230 type dilatometer was applied to study the thermal dilatation behavior and to determine the transition temperature. The dilatometer measurement was carried out in air applying a heating rate of 10 K/min. The initial length of the cylindrical sample was $l_0 = 5.220$ mm. The obtained data are presented in Fig. 7. The value of the physical coefficient of expansion was calculated with the relation: $\alpha = (1/l_t)(\mathrm{d}(l_t - l_0)/\mathrm{d}t)$, where l_0 and l_t are the sample length at initial and high temperatures, and t is the temperature.

Data availability

The data that support the findings of this study are available from the corresponding authors upon a reasonable request.

Received: 4 July 2018 Accepted: 11 March 2019
Published online: 02 May 2019

References

1. Yeh, J.-W. et al. Nanostructured high-entropy alloys with multiple principal elements: novel alloy design concepts and outcomes. *Adv. Eng. Mater.* **6**, 299–303 (2004).
2. Cantor, B., Chang, I. T. H., Knight, P. & Vincent, A. J. B. Microstructural development in equiatomic multicomponent alloys. *Mater. Sci. Eng. A* **375–377**, 213–218 (2004).
3. Gludovatz, B. et al. A fracture-resistant high-entropy alloy for cryogenic applications. *Science* **345**, 1153–1158 (2014).
4. Zou, Y., Ma, H. & Spolenak, R. Ultrastrong ductile and stable high-entropy alloys at small scales. *Nat. Commun.* **6**, 7748 (2015).
5. Youssef, K. M., Zaddach, A. J., Niu, C., Irving, D. L. & Koch, C. C. A novel low-density, high-hardness, high-entropy alloy with close-packed single-phase nanocrystalline structures. *Mater. Res. Lett.* **3**, 95–99 (2015).
6. Lee, C. P., Chen, Y. Y., Hsu, C. Y., Yeh, J. W. & Shih, H. C. The effect of boron on the corrosion resistance of the high entropy alloys $Al_{0.5}CoCrCuFeNiB_x$. *J. Electrochem. Soc.* **154**, C424–C430 (2007).
7. Guo, J. et al. Robust zero resistance in a superconducting high-entropy alloy at pressures up to 190 GPa. *Proc. Natl Acad. Sci.* **114**, 13144–13147 (2017).
8. Zhang, Y., Zuo, T., Cheng, Y. & Liaw, P. K. High-entropy alloys with high saturation magnetization, electrical resistivity, and malleability. *Sci. Rep.* **3**, 1455 (2013).
9. Koželj, P. et al. Discovery of a superconducting high-entropy alloy. *Phys. Rev. Lett.* **113**, 107001 (2014).
10. Yao, Y. et al. Carbothermal shock synthesis of high-entropy-alloy nanoparticles. *Science* **359**, 1489–1494 (2018).
11. Zhang, Y. et al. Microstructures and properties of high-entropy alloys. *Prog. Mater. Sci.* **61**, 1–93 (2014).
12. Ye, Y. F., Wang, Q., Lu, J., Liu, C. T. & Yang, Y. High-entropy alloy: challenges and prospects. *Mater. Today* **19**, 349–362 (2016).
13. Miracle, D. B. & Senkov, O. N. A critical review of high entropy alloys and related concepts. *Acta Mater.* **122**, 448–511 (2017).
14. Guillaume, C. E. Recherches sur les aciers au nickle. Dilatations aux températures élevées; résistance électrique. *C. R. Acad. Sci.* **125**, 235–238 (1897).
15. Weiss, R. J. The origin of the 'Invar' effect. *Proc. Phys. Soc.* **82**, 281–288 (1963).
16. Van Schilfgaarde, M., Abrikosov, I. A. & Johansson, B. Origin of the Invar effect in iron-nickel alloys. *Nature* **400**, 46–49 (1999).
17. Dubrovisky, L. et al. Pressure-induced Invar effect in Fe-Ni alloys. *Phys. Rev. Lett.* **86**, 4851–4854 (2001).
18. Rueff, J. P. et al. Magnetism of Invar alloys under high pressure examined by inelastic x-ray scattering. *Phys. Rev. B* **63**, 132409 (2001).
19. Decremps, F. & Nataf, L. Abrupt discontinuity of the bulk modulus pressure dependence in $Fe_{64}Ni_{36}$. *Phys. Rev. Lett.* **92**, 157204 (2004).
20. Zeng, Q. S. et al. Anomalous compression behavior in lanthanum/cerium-based metallic glass under high pressure. *Proc. Natl Acad. Sci.* **104**, 13565–13568 (2007).
21. Singh, A. K. X-ray diffraction from solids under nonhydrostatic compression-some recent studies. *J. Phys. Chem. Solids* **65**, 1589–1596 (2004).
22. Nogués, J. et al. Volume expansion contribution to the magnetism of atomically disordered intermetallic alloys. *Phys. Rev. B* **74**, 024407 (2006).
23. Huang, S. et al. Mechanism of magnetic transition in FeCrCoNi-based high entropy alloys. *Mater. Des.* **103**, 71–74 (2016).
24. Niu, C., LaRosa, C. R., Miao, J., Mills, M. J. & Ghazisaeidi, M. Magnetically-driven phase transformation strengthening in high entropy alloys. *Nat. Commun.* **9**, 1363 (2018).
25. Zuo, T. et al. Tailoring magnetic behavior of CoFeMnNiX (X = Al, Cr, Ga, and Sn) high entropy alloys by metal doping. *Acta Mater.* **130**, 10–18 (2017).
26. Poirier, J.-P. *Introduction to the Physics of the Earth's Interior* (Cambridge University Press, Cambridge, 2000).
27. Fakirov, S. On the application of the "rule of mixture" to microhardness of complex polymer systems containing a soft component and/or phase. *J. Mater. Sci.* **42**, 1131–1148 (2007).
28. Mollaev, A. Y. et al. Anomalies of magnetic properties and magnetovolume effect in $Cd_{1-x}Mn_xGeAs_2$ at hydrostatic pressure. *Appl. Phys. Lett.* **100**, 202403 (2012).
29. Gorria, P. et al. Crystal structure, magnetocaloric effect and magnetovolume anomalies in nanostructured Pr_2Fe_{17}. *Acta Mater.* **57**, 1724–1733 (2009).
30. Zhang, F. et al. Polymorphism in a high-entropy alloy. *Nat. Commun.* **8**, 15687 (2017).
31. Tracy, C. M. et al. High pressure synthesis of a hexagonal close-packed phase of the high-entropy alloy CrMnFeCoNi. *Nat. Commun.* **8**, 15634 (2017).
32. Zhang, F. X. et al. Pressure-induced fcc to hcp phase transition in Ni-based high entropy solid solution alloys. *Appl. Phys. Lett.* **110**, 011902 (2017).

33. Tsai, K. Y., Tsai, M. H. & Yeh, J. W. Sluggish diffusion in Co–Cr–Fe–Mn–Ni high-entropy alloys. *Acta Mater.* **61**, 4887–4897 (2013).
34. Martin, N. et al. Magnetovolume effect, macroscopic hysteresis and moment collapse in the paramagnetic state of cubic MnGe under high pressure. *Phys. Rev. B* **93**, 214404 (2016).
35. Machon, D., Meersman, F., Wilding, M. C., Wilson, M. & McMillan, P. F. Pressure-induced amorphization and polyamorphism: inorganic and biochemical systems. *Prog. Mater. Sci.* **61**, 216–282 (2014).
36. Dewaele, A., Torrent, M., Loubeyre, P. & Mezouar, M. Compression curves of transition metals in the Mbar range: experiments and projector augmented-wave calculations. *Phys. Rev. B* **78**, 104102 (2008).
37. Liermann, H.-P. et al. The extreme conditions beamline P02.2 and the extreme conditions science infrastructure at PETRA III. *J. Synchrotron Radiat.* **22**, 908–924 (2015).
38. Zhang, D. et al. High pressure single crystal diffraction at PX^2. *J. Vis. Exp.* **119**, e54660 (2017).
39. Fei, Y. et al. Toward an internally consistent pressure scale. *Proc. Natl Acad. Sci.* **104**, 9182–9186 (2007).
40. Prescher, C. & Prakapenka, V. B. DIOPTAS: a program for reduction of two-dimensional X-ray diffraction data and data exploration. *High Press. Res.* **35**, 223–230 (2015).
41. Wojdyr, M. Fityk: a general-purpose peak fitting program. *J. Appl. Crystallogr.* **43**, 1126–1128 (2010).
42. Gonzalez-Platas, J., Alvaro, M., Nestola, F. & Angel, R. EosFit7-GUI: a new graphical user interface for equation of state calculations, analyses and teaching. *J. Appl. Cryst.* **49**, 1377–1382 (2016).
43. Hohenberg, P. & Kohn, W. Inhomogeneous electron gas. *Phys. Rev.* **136**, B864–B871 (1964).
44. Vitos, L. *Computational Quantum Mechanics for Materials Engineers* (Springer, London, 2007).
45. Vitos, L. Total-energy method based on the exact muffin-tin orbitals theory. *Phys. Rev. B* **64**, 014107 (2001).
46. Perdew, J. P., Burke, K. & Ernzerhof, M. Generalized gradient approximation made simple. *Phys. Rev. Lett.* **77**, 3865–3868 (1996).
47. Soven, P. Coherent-potential model of substitutional disordered alloys. *Phys. Rev.* **156**, 809–813 (1967).
48. Gyorffy, B. L. Coherent-potential approximation for a nonoverlapping-muffin-tin-potential model of random substitutional alloys. *Phys. Rev. B* **5**, 2382–2384 (1972).
49. Vitos, L., Abrikosov, I. A. & Johansson, B. Anisotropic lattice distortions in random alloys from first-principles theory. *Phys. Rev. Lett.* **87**, 156401 (2001).
50. Gyorffy, B. L., Pindor, A. J., Staunton, J., Stocks, G. M. & Winter, H. A first-principles theory of ferromagnetic phase transitions in metals. *J. Phys. F Met. Phys.* **15**, 1337–1386 (1985).
51. Skubic, B., Hellsvik, J., Nordström, L. & Eriksson, O. A method for atomistic spin dynamics simulations: implementation and examples. *J. Phys. Condens. Matter* **20**, 315203 (2008).

Acknowledgements

This research was supported by Uppsala University and by the National Natural Science Foundation of China (No. 11504354). S.H. and L.V. acknowledge the Swedish Research Council (VR), the Swedish Foundationfor Strategic Research (SSF), and the Swedish Energy Agency. L.V. and L.K.V. acknowledge the Hungarian Scientific Research Fund (OTKA 128229). The computations were performed on resources provided by the Swedish National Infrastructure for Computing (SNIC) at Linköping. Parts of this research were carried out at the light source PETRA III at DESY, a member of the Helmholtz Association (HGF). Parts of studies were performed at GSECARS (The University of Chicago, Sector 13), Advanced Photon Source (APS), Argonne National Laboratory. GSECARS is supported by the National Science Foundation—Earth Sciences (EAR-1634415) and Department of Energy-GeoSciences (DE-FG02–94ER14466). Use of the COMPRES-GSECARS gas loading system was supported by COMPRES under NSF Cooperative Agreement EAR-1606856 and by GSECARS through NSF grant EAR-1634415 and DOE grant DE-FG02–94ER14466. The PX^2 program is supported by COMPRES under NSF Cooperative Agreement EAR-1661511. This research used resources of the Advanced Photon Source, a U.S. Department of Energy (DOE) Office of Science User Facility operated for the DOE Office of Science by Argonne National Laboratory under Contract No. DE-AC02–06CH11357.

Author contributions

L.L. and P.L. conceived the project. L.L., P.L., M.D., E.B. and D.Z. performed the synchrotron XRD measurements with help from J.-E.R., S.H. and L.V. carried out the theoretical calculation. B.S.G.A. and L.L. conducted the magnetic measurement. S.I. characterized the sample. B.V. and L.K.V. measured the CTE of the sample. L.L., P.L., S.H. and L.V. analyzed the data and drafted the manuscript. All authors contributed to the discussions and comments on the final manuscript.

Additional information

Supplementary information accompanies this paper at https://doi.org/10.1038/s42005-019-0141-9.

Competing interests: The authors declare no competing interests.

Reprints and permission information is available online at http://npg.nature.com/reprintsandpermissions/

Publisher's note: Springer Nature remains neutral with regard to jurisdictional claims in published maps and institutional affiliations.